Tectonophysics 712–713 (2017) 589–599

Contents lists available at ScienceDirect

Tectonophysics

journal homepage: www.elsevier.com/locate/tecto

Permeability and permeability anisotropy in Crab Orchard sandstone: Experimental insights into spatio-temporal effects

Stephan Gehne *, Philip M. Benson

University of Portsmouth, Rock Mechanics Laboratory, School of Earth and Environmental Sciences, Portsmouth, United Kingdom

ARTICLE INFO

Article history:
Received 16 March 2017
Received in revised form 6 June 2017
Accepted 9 June 2017
Available online 17 June 2017

Keywords:
Velocity and permeability anisotropy in Crab Orchard sandstone
Time dependent permeability recovery
Stress path dependent permeability recovery
Initial pressure cycles dictate the subsequent recoverability
Anisotropy of permeability, strain, and P-wave elastic velocity

ABSTRACT

Permeability in tight crustal rocks is primarily controlled by the connected porosity, shape and orientation of microcracks, the preferred orientation of cross-bedding, and sedimentary features such as layering. This leads to a significant permeability anisotropy. Less well studied, however, are the effects of time and stress recovery on the evolution of the permeability hysteresis which is becoming increasingly important in areas ranging from fluid migration in ore-forming processes to enhanced resource extraction. Here, we report new data simulating spatio-temporal permeability changes induced using effective pressure, simulating burial depth, on a tight sandstone (Crab Orchard). We find an initially (measured at 5 MPa) anisotropy of 2.5% in P-wave velocity and 180% in permeability anisotropy is significantly affected by the direction of the effective pressure change and cyclicity; anisotropy values decrease to 1% and 10% respectively after 3 cycles to 90 MPa and back. Furthermore, we measure a steadily increasing recovery time (10–20 min) for flow parallel to cross-bedding, and a far slower recovery time (20–50 min) for flow normal to cross-bedding. These data are interpreted via strain anisotropy and accommodation models, similar to the "seasoning" process often used in dynamic reservoir extraction.

© 2017 The Authors. Published by Elsevier B.V. This is an open access article under the CC BY license (http://creativecommons.org/licenses/by/4.0/).

Key points

- Velocity and permeability anisotropy in Crab Orchard Sandstone
- Time dependent permeability recovery
- Stress path dependent permeability recovery
- Initial pressure cycles dictate the subsequent recoverability
- Anisotropy of permeability, strain, and P-wave elastic velocity

1. Introduction

The permeability of rock is a key physical property, describing the ability of pore fluid to move within a rock mass (Guéguen and Palciauskas, 1994). It is of critical importance in both fundamental and applied geosciences, from oil and gas extraction to foundation engineering, hydrology and environmental science. For the economic extraction of oil and gas, high recovery rates are needed which are highly dependent on the permeability of the reservoir rock, amongst other parameters (e.g. porosity). However, due to new advances in directional drilling and reservoir stimulation technologies, tight gas and tight oil have now become a substantial source for hydrocarbons. Unlike conventional reservoirs, these reserves are contained within low permeability ($<20 \times 10^{-15}$ m^2) sedimentary rock lithologies such as shale and so-called tight (cemented) sandstone and carbonate rocks (e.g. Bennion et al., 1996). For the successful extraction of these hydrocarbons it is necessary to understand the complex physics of fluid flow in low permeability rock. This is not trivial, as a range of factors, such as stress history and effective pressure dependence, may significantly alter the fluid conductivity of the rock. Such a phenomenon was reported by Keaney et al. (1998), who investigated the evolution of axial permeability of Tennessee Crab Orchard Sandstone (COS) under hydrostatic conditions as a function of increasing compressive differential stress. These early results showed a pronounced stress-history dependency of permeability and sensitivity to effective pressure.

Stress-history dependency, also known as hysteresis or path dependency, refers to the influence of past stress states on rock properties (Spiteri et al., 2008). A range of studies have investigated path dependency as a function of rock strength, strain, dilatancy and permeability (Zoback and Byerlee, 1975a; Hadley, 1976; Scholz and Koczynski, 1979). These effects are well known in rock mechanics studies, and to minimise their negative effects a practice named "seasoning" may be applied (Bernabé, 1987). During seasoning, the sample is subjected to several cycles of increasing and decreasing effective pressure. Selvadurai and Glowacki (2008) subjected a sample of Indiana limestone to several cycles of increasing and decreasing compressive isostatic confining pressure. Their results indicated an irreversible reduction of hydraulic conductivity with increasing pressure conditions. Experiments by Brace et al. (1968) on Westerly Granite (USA); by Lion et al. (2004) on a high porosity and permeability limestone from Anstrude (France); and by David et al. (2001) on high porosity Rothbach

* Corresponding author.
E-mail address: stephan.gehne@port.ac.uk (S. Gehne).

http://dx.doi.org/10.1016/j.tecto.2017.06.014
0040-1951/© 2017 The Authors. Published by Elsevier B.V. This is an open access article under the CC BY license (http://creativecommons.org/licenses/by/4.0/).

sandstone (France), all showed a strong reduction of permeability with increasing confining pressure. Shiping et al. (1994) showed that the fluid permeability of rocks is a function of strain, concluding that permeability must be closely related to the stress field, a conclusion also reached by other researchers (Zoback and Byerlee, 1975b; Bai et al., 1999; Wang and Xu, 2013). From these investigations, it becomes clear that the deformation of the specimen needs be taken into account when analysing the evolution of permeability.

However, complicating the situation further, fluid permeability is also influenced by anisotropy present in the rock mass (or sample): either inherent to the rock type or induced due to the stress state. A medium is characterised as anisotropic when its properties change with measurement direction (Amadei, 1982). For permeability, this refers to the magnitude of fluid flow as a function of the flow direction through the sample with respect to layering, or small scale heterogeneities (Meyer, 2002). Furthermore, permeability anisotropy is also stress-dependent, as reported by Jones et al. (1998) who compared the permeability anisotropy of a shale, sandstone and tuff. Taking this a step further, hysteresis generated due to pressure cycling represents a superposition of many inter-related time-dependent elastic effects. These effects range in scope from short term elasticity, in which rock deformation may be fully recoverable; mid-term anelastic deformation, whereby a deformation may recover through extended periods of time; to inelastic deformation, where the damage to the rock is permanent and is never recovered in any length of time. Thus, a rock retrieved from its natural environment (and under test in the laboratory, for example) has already been 'damaged' to an extent, due to the removal from its in-situ pressure conditions. It is therefore reasonable to assume that any representative volume of rock mass has already been transited through a complex stress-time history due to geological burial/uplift, and/or modification of pore pressure over time both naturally and due to artificial means (resource extraction).

For this reason, it is useful to understand time and stress dependent influence on rock permeability, and whilst it is impossible to relate the properties of a rock sample recovered at depth and tested in the lab under different conditions, it is possible to measure how rock properties vary as a function of cyclical hydrostatic stresses in a holistic manner. This is important, as a large number of fundamental and applied research depends on understanding fluid flow properties at depth where pressures and stresses change dynamically, such as in reservoirs producing oil and gas, and during hydraulic fracturing to produce shale oil/gas. These problems are further complicated by the fact that crustal stresses are inherently anisotropic. Therefore, linking laboratory scale measurements and mechanisms to those relevant at field scale remains crucial, but challenging. Despite this, new laboratory experiments targeting the temporal change in mechanical and fluid transport properties as a function of an externally applied fluid pressure or stress have great potential to better understand these dependencies – especially in terms of recovery time – in shallow reservoir conditions.

Here, we report new data from a laboratory study where the effect of stress-history, effective pressure and anisotropy is correlated to fluid permeability and permeability anisotropy. This is achieved by applying pressure cycles over a range from 2.5 MPa to 90 MPa and recording the evolution of permeability, porosity, axial strain, and elastic-wave velocity. This reveals a complex time dependent response of the rock fabric to the hydrostatic pressure, including a strong permeability hysteresis effect.

2. Sample material, characteristics and preparation

The material studied is Crab Orchard Sandstone (COS), chosen due to its low porosity and anisotropic character, both in terms of elastic wave anisotropy and permeability anisotropy. This material, from the Cumberland Plateau, Tennessee, USA, is a fine grained, cross bedded fluvial sandstone (Benson et al., 2003) with a very low water porosity of approximately 5%. The helium gas porosity is approximately 10%. The grains range from subhedral to subrounded, are approx. 0.25 mm in size and generally without a preferred alignment. It exhibits mm scale cross-bedding and is highly anisotropic (20% P-wave velocity anisotropy). The rock consists predominantly of quartz (>85%) with minor contents of feldspar and lithics and cemented by sericitic clay (Benson et al., 2003; Benson et al., 2006). The sandstone has very low bulk permeability in the micro-darcy range (10^{-18} m^2). Analysis via scanning electron microscopy (Fig. 1) illustrates the microstructure, which consists of pore spaces filled with cement and clays. XRD analysis of the cement indicates a mixture of Illite, Kaolinite and Chlorite.

3. Experimental equipment and methods (elevated isostatic pressures)

All test samples were cored from the same block of rock to minimise the effect of sample heterogeneity. A radial arm drilling machine was used for the coring process, followed by cutting and grinding the ends of the sample to achieve a parallelism of ± 0.1 mm using a lathe, fitted with a cross cutting end grinder. Rock samples were cored in two orthogonal directions; in the X-direction the coring axis is parallel to bedding and in the *Z*-direction the coring axis is normal to bedding, which are referred to as COS_x and COS_z respectively. The suffixes "x" (parallel) and "z" (normal) indicate the direction relative to the visual bedding planes. Experiments were conducted on cylindrical specimens measuring approx. 40 mm (± 0.1 mm) in diameter and 100 mm (± 0.1 mm) in length.

Samples were first vacuum saturated with distilled water for a minimum of 24 h. The permeability experiments were then performed using a triaxial deformation cell operating in hydrostatic mode. The apparatus incorporates an oil-medium pressure chamber and two servo-controlled pumps to independently generate axial stress and confining pressure, synchronised electronically to provide an isostatic stress field. Fig. 2 shows a schematic of the equipment. The axial pressure is applied via a hydraulically driven piston. Two additional servo-controlled pumps independently supply high-pressure pore fluid (distilled water) to both ends of the test sample. Each pump can be separated from the circuit by electronically operated valves, which enables the sample to be subjected to an isostatic pressure of up to 100 MPa as well as to fluid flow through the specimen at a known hydraulic gradient. The sample is separated from the confining oil through an engineered rubber jacket which also holds 12 acoustic emission (AE) sensors, evenly distributed over the sample (Sammonds, 1999).

The following experimental protocol was followed for experiments on separate samples cut parallel and normal to bedding in order to assess anisotropic effects. All samples were pressurised by applying a small differential pore pressure between the two ends of the sample (0.4–0.8 MPa) at an effective pressure of 3 MPa. The effective pressure

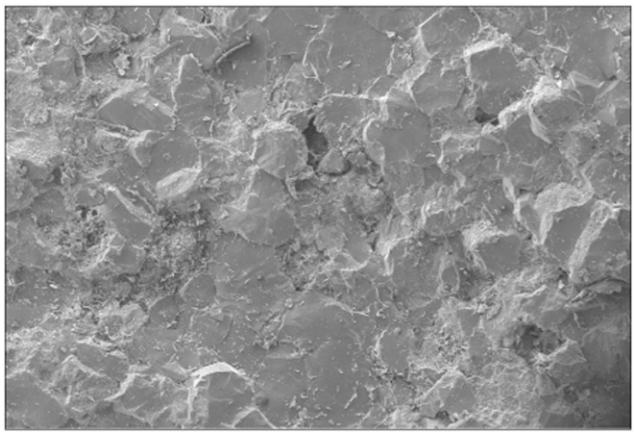

Fig. 1. Scanning electron micrograph image of Crab Orchard sandstone, showing a pervasive networks of both angular pore space, and crack fabric.

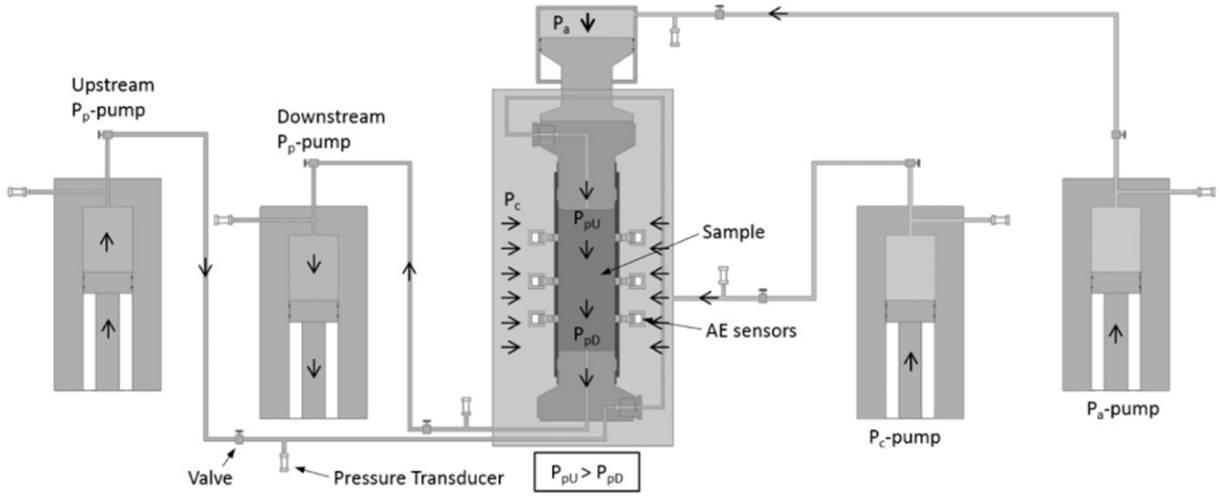

Fig. 2. Schematic diagram of triaxial deformation cell used for simultaneous permeability, porosity, axial strain and acoustic wave velocity measurements; fluid/pore pressure upstream (P_{pU}), fluid/pore pressure downstream (P_{pD}).

is given by the effective pressure law $P_{eff} = P_c - \alpha * P_p$, where P_{eff} is the effective confining pressure, Pc the externally applied confining pressure, Pp the applied pore pressure and α the Biot effective stress parameter, a poro-elastic constant. For this study, the simple effective pressure law is assumed where $\alpha = 1$ (Keaney et al., 2004). Full saturation was assumed once the downstream pump started receiving pore fluid. For COS, this took between 12 and 24 h depending on the orientation of the bedding. During the experiment, permeability was measured under changing effective pressure conditions up to 90 MPa via steady-state flow and Darcy's law. The average pore pressure was kept constant, whereas the isotropic compressive stresses were increased/decreased in increments of 5 and 10 MPa. A mean fluid pressure of around 5 MPa was set, with a constant pressure gradient of 0.4–0.8 MPa across the sample. Fluid flow through the samples from the upstream to the downstream pore fluid pump was directly measured via the reservoir volume change as a function of time. Permeability anisotropy was determined by flowing fluid through COS samples, one with fluid flow parallel and one with fluid flow normal to visually determined bedding planes. Four pressure cycles of increasing and decreasing effective pressure (Confining pressure P_c − Pore Pressure P_p) were applied over a range from 5 MPa to 90 MPa. At each pressure step, permeability (k), elastic P-wave velocities (V_P), porosity (P) and axial strain (ε_a) are recoded concomitantly for later analysis.

In a typical test sequence, samples were subjected to four pressure cycles. During each cycle, the effective pressure was first increased and then decreased stepwise between 2.5 and 90 MPa in steps of 5 MPa (from 5 to 20 MPa) thereafter steps of 10 MPa. After each change in effective pressure, the pore-fluid system was allowed to equilibrate to the new pressure conditions and establish a new steady flow. The time this takes is derived from plotting the reservoir volumes over time (Fig. 3), where a break in slope indicates when equilibrium is re-established. In case of increasing hydrostatic pressure, the sample first drains as shown by increasing volumes in both reservoirs (Fig. 3a). The break in slope then indicates that equilibrium is attained and volume in the upstream reservoir will decrease at a similar flow rate as the downstream volume increases (confirming no leaks in the system). In the second case, where pressure is decreased (Fig. 3b), the data shows decreasing volume in both reservoirs. Both pumps, upstream and downstream, initially inject water into the sample as pore space opens up due to pressure release, which is filled by the pore fluid. Once more, equilibrium is then indicated by a break in slope in both curves, as the upstream reservoir volume continues to decrease at a lower rate and the downstream reservoir volume starts to increase, receiving pore fluid. This behaviour is typical for a fluid saturated, low permeability rock (Jones et al., 1998) and was more obvious with the fluid flow normal to bedding.

A minimum of 30 min is permitted to ensure stable flow rates and a steady-state flow through the sample before permeability measurements are taken (over a 20–30 min period). The permeability was calculated for each effective pressure step using the steady-state-flow technique. By applying Darcy's Law, permeability is calculated directly from the fluid flow rate, pressure gradient and the sample dimensions using the following expression (Jones et al., 1998; Benson, 2004):

$$k = \frac{4^{*}\frac{dV^{*}}{dt}\eta^{*}L}{\pi^{*}d^{2^{*}}(P_U - P_D)}$$

where: k = Permeability (m^2)
dV/dt = flow rate (m^3/s)
η = viscosity of water (Pa.s)
L = sample length (m)
D = sample diameter (m)
P_U = Fluid pressure at Upstream end of sample (Pa)
P_D = Fluid pressure at Downstream end of sample (Pa)

During confining pressure increase/decrease, the volume change in the upstream and downstream reservoirs is also used as an indirect measure of water expulsion/injection due to closure/opening of cracks and pores. This translates into a porosity change with changing effective pressure (Benson et al., 2005). All mechanical/pressure data (axial stress, confining pressure, pore pressures and reservoir volumes) were recorded and logged continuously at 10 s intervals. In addition, acoustic emission data were recorded and compressional wave velocities were measured every 5 min at each effective pressure step using a 12 sensor array via the time-of flight technique. Permeability and elastic wave velocity anisotropies have been calculated with the general formula $A_k = 100\% * ((k_{max} - k_{min}) / k_{mean})$ and $A_v = (V_{max} - V_{min}) / V_{mean}$ respectively, where A_k and A_v are anisotropy parameters (Benson, 2004; Benson et al., 2005).

In addition to the P-wave data collected under hydrostatic pressure, P-wave elastic velocities at ambient pressure conditions were also collected to determine the basic anisotropy of the "as-collected" materials. These were made under dry conditions diametrically as a function of azimuth every 10° around the cylindrical samples, as well as axially (Jones et al., 1998; Benson et al., 2003). The same standard (40 mm diameter) cores, and in both X- and *Z*- directions, were used for this, allowing the maximum anisotropy to be evaluated. To minimise scattering effects,

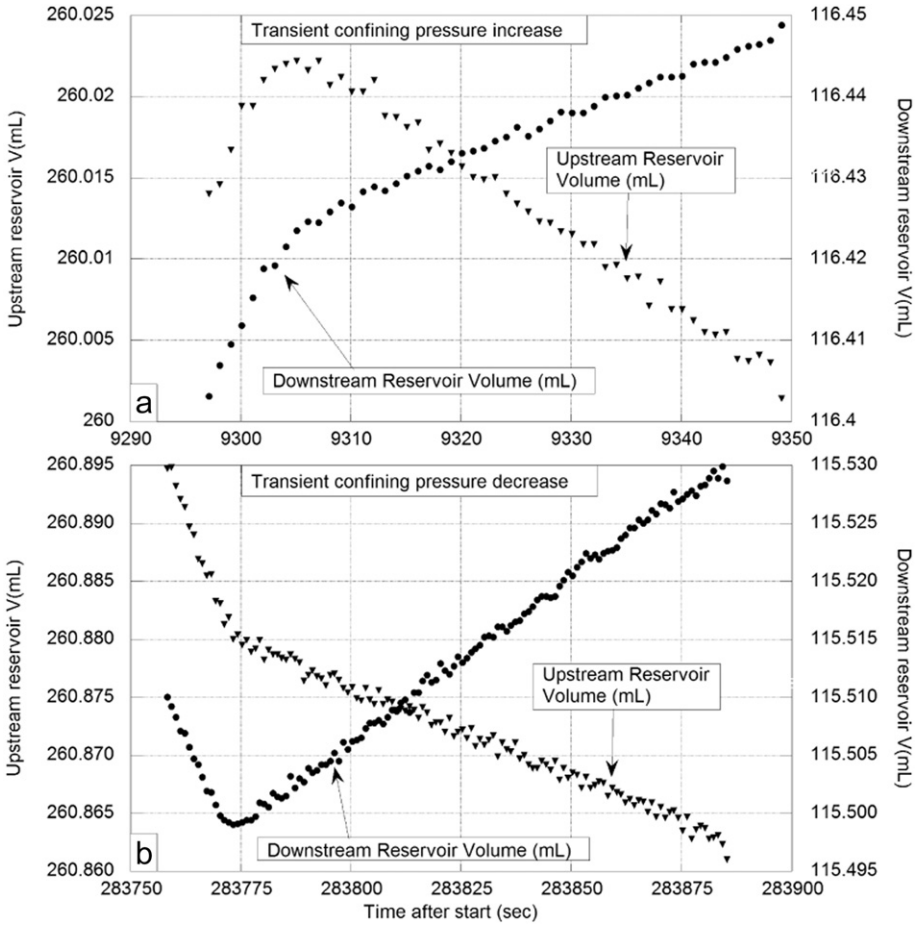

Fig. 3. Example raw data for reservoir volume over time in the case for (a) a transient increase in the effective pressure, resulting in downstream flow rate decrease, and matched by an equal but opposite flow rate in upstream reservoir. For (b) a transient decrease in effective pressure where the reverse effect is seen.

transducers with a central frequency of 1 MHz were used (Panametrics V103). Therefore, the wavelength corresponded to approximately ten grain diameters and the sample size was greater than ten wavelengths (Benson et al., 2005).

4. Results

4.1. Acoustic wave velocity measurements at ambient pressure

Compressional wave velocities were measured on 3 samples for each of the two directions. The maximum velocity (3653 m/s) was measured parallel to the cross-bedding and the minimum (2754 m/s) perpendicular to the cross-bedding. The directional dependence of wave velocity indicates an anisotropic character of the sandstone yielding a V_P-anisotropy at ambient pressure conditions (A_{Va}) of 19% (Fig. 4).

4.2. Strength and strain measurements at elevated pressure

The strength and key mechanical properties of COS were measured as part of the study, as a matter of routine. These data are reported in Table 1 for samples orientated with principal stress maximum both parallel and normal to the inherent bedding.

Mechanical properties vary considerably depending on the relative orientation of the imposed strain (deformation) with respect to the cross-bedding. Whereas COS_x failed at a differential stress of 174.1 MPa and with a Young's Modulus of 49.3 GPa; COS_z failed at 208.9 MPa with a Young's Modulus of 43.9 GPa. This results in a strength anisotropy of 18%. Comparing the deformation behaviour of the two samples reveals that COS_x possesses a higher maximum diametric strain (0.45% compared to 0.25%), whereas the opposite is measured for axial strain (0.8% for COS_z compared to 0.4% for COS_x). This results in a

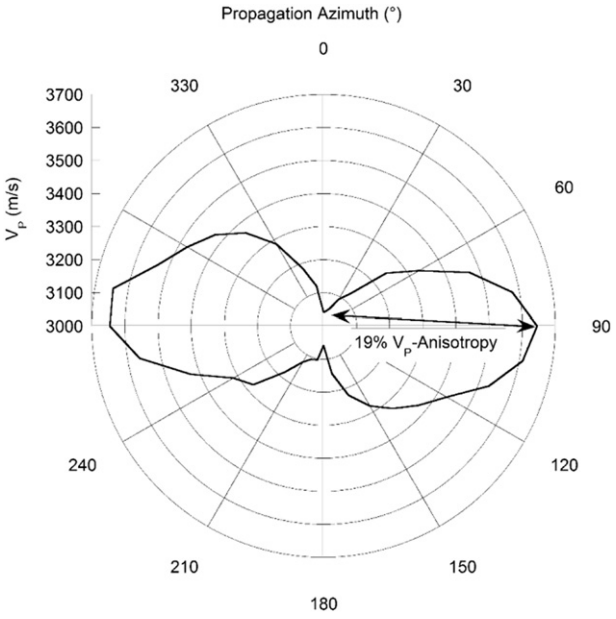

Fig. 4. Average compressional elastic wave velocities measured across the diameter under ambient and dry conditions at 10° intervals, indicating V_P-Anisotropy.

Table 1
Physical and mechanical properties of COS deformed at elevated confining pressure (8 MPa).

	COS_x	COS_z	Anisotropy
Max. differential stress at failure (MPa)	174.1	208.9	~18%
Young's modulus (GPa)	49.3	43.9	
Poisson's ratio	0.31	0.11	
Max. axial strain at failure (%)	0.4	0.8	~67%
Max. diametric strain at failure (%)	0.45	0.25	~57%

significant difference in the Poisson's ratio for the two deformation directions relative to bedding: 0.31 for COS_x compared to 0.11 for COS_z.

4.3. Fluid flow and acoustic wave velocity measurements under elevated hydrostatic pressure

Permeability and compressional wave velocities were measured concomitantly at effective hydrostatic pressures from 2.5 to 90 MPa. This was repeated for cores with the axis parallel and normal to bedding to derive the anisotropy. After each pressure change, the system was allowed to establish equilibrium and a steady flow to be re-established before permeability and elastic wave velocity measurements were taken. Equilibrium was considered to be attained once the upstream and downstream reservoirs are delivering and receiving at similar but opposite flow rates (indicating no leaks in the system). Changes in sample porosity with changing effective pressure were also determined from the recorded volume of the pore fluid reservoirs. For both flow directions, a permanent reduction of porosity has been caused by the pressure cycling: P_x reduced from 3.8% initially to 1.5% and P_z from 4.5% to 3.9% (Fig. 5a and c). Porosity significantly reduces in COS_x (P_x) during the 1st cycle, decreasing from initially 3.8% at 0 MPa to 1.5% at 90 MPa. During the first cycle, the majority of this change occurs rapidly early in the pressurisation, becoming almost linear above approximately 20 MPa. This "linear" trend is subsequently seen for the following pressure cycles. As effective pressure is decreased again, porosity does recover slightly, but not to its original value. The main reduction in porosity occurs for fluid flow normal to bedding (P_z) in cycle 1 and to a lesser extent in cycle 2 (Fig. 5c). Porosity decreases in the 1st cycle from initially 4.5% at 0 MPa to 3.95% at 90 MPa and in the 2nd cycle from 4.1% at 2.5 MPa to 3.7% at 70 MPa. Beyond this pressure point, however, almost no additional reduction occurs and in both cycles, the porosity does not return to its initial value. The subsequent cycles still show a reduction in porosity (from 3.9% to around 3.7%) when increasing effective pressure, but without permanent reduction as it follows the same path as it recovers when effective pressure is decreased again. COS_z shows a linear and gradual reduction in porosity over all pressure cycles. As the absolute porosity is not affected by the

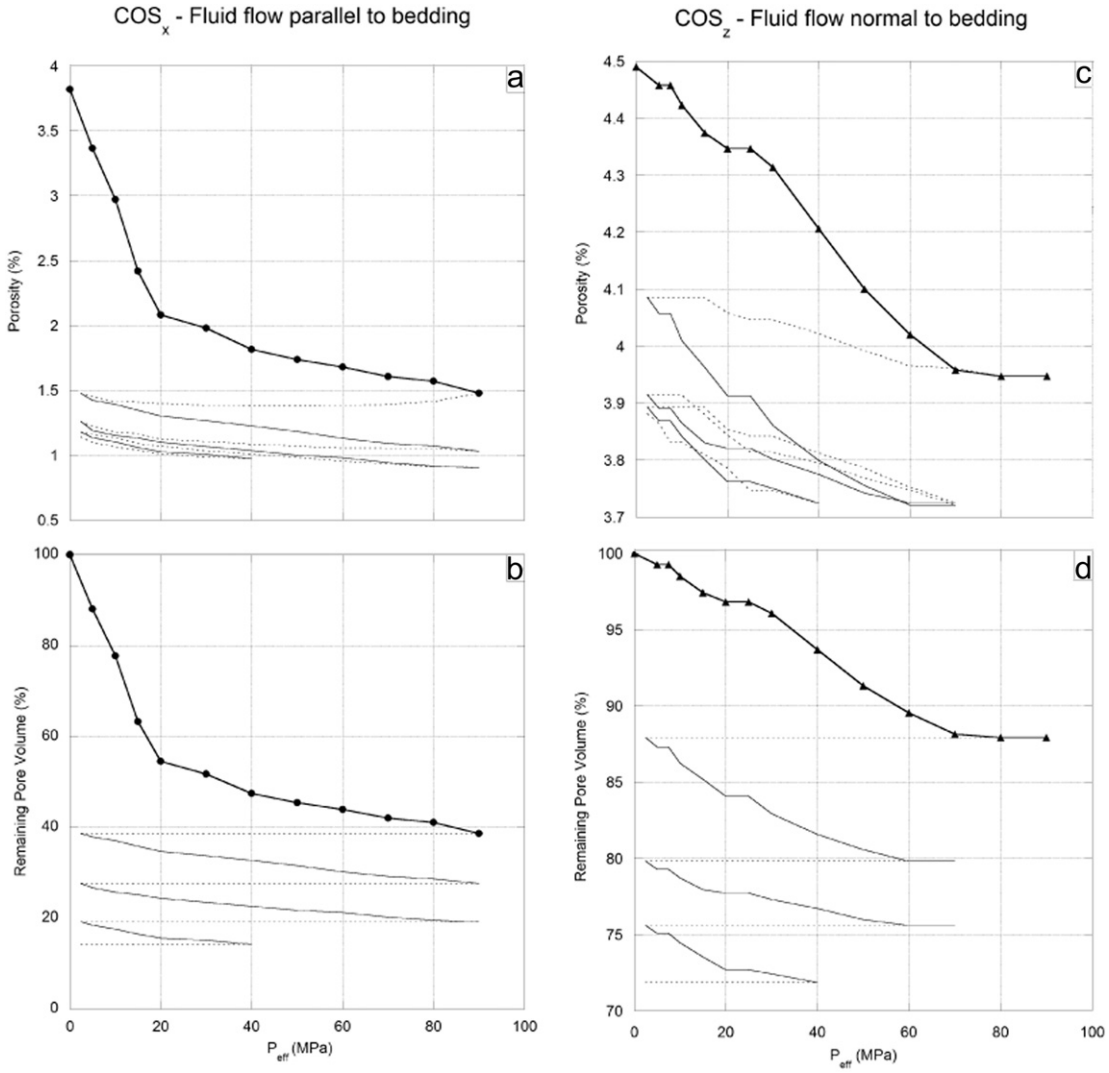

Fig. 5. Evolution of porosity (upper panels (a) and (c)) and pore volume change (lower panels (b) and (b)) for fluid flow parallel to bedding (panels (a) and (b), left) and normal to bedding (panels (c) and (d), right) – for increasing effective pressure (solid lines), and decreasing effective pressure (dotted lines).

orientation of the bedding, but can vary between samples, we also considered the remaining open pore volume as a function of effective pressure to compare both samples (Fig. 5b and d). This shows the same reduction pattern as described above for COS_x and COS_z: a continuous reduction of the open pore volume, but with significant differences in the magnitude. After the pressure cycling, only 15% of the pores remained open in COS_x, whereas 70% of the pore network remained intact in COS_z.

Fig. 6 presents elastic wave velocities relative to bedding, and as a function of changing effective pressure (Table 2). During these experiments, elastic wave measurements were made across the sample diameter by pulsing each sensor in sequence and receiving the pulse on the remaining 11 receivers, choosing ray paths most closely aligned normal or parallel to the crossbedding. Most of the velocity increase occurs at effective pressures below 40 MPa, with the rate of increase slowing above this point independently of wave propagation direction and sample. Wave velocities measured for COS_x enable P-wave data to be collected both parallel and normal to the bedding plane, as the 12-sensor array includes a "plane" of sensors with pairs at 90 to each other, and aligned to the bedding orientated axially. Fig. 6 summarises this setup, showing V_{PX} increasing by approximately 700 m/s parallel and 800 m/s normal to bedding (Fig. 6a). Using these two values, a velocity anisotropy (A_v) is calculated of approximately 2.8% (128 m/s) at 2.5 MPa, which decreases to 0.2% (12 m/s) at 90 MPa (Fig. 6b). It is also clear that V_P does not return to its initial value (Fig. 6a). Instead, an irreversible velocity increase occurs of approximately 50 m/s (1.1% of starting value) and 30 m/s (0.7%) respectively for both directions after the pressure cycling ceases. The permanent change is mainly measured during the first cycle with subsequent cycles of effective pressure change following nearly the same path. The measured velocities are stated below.

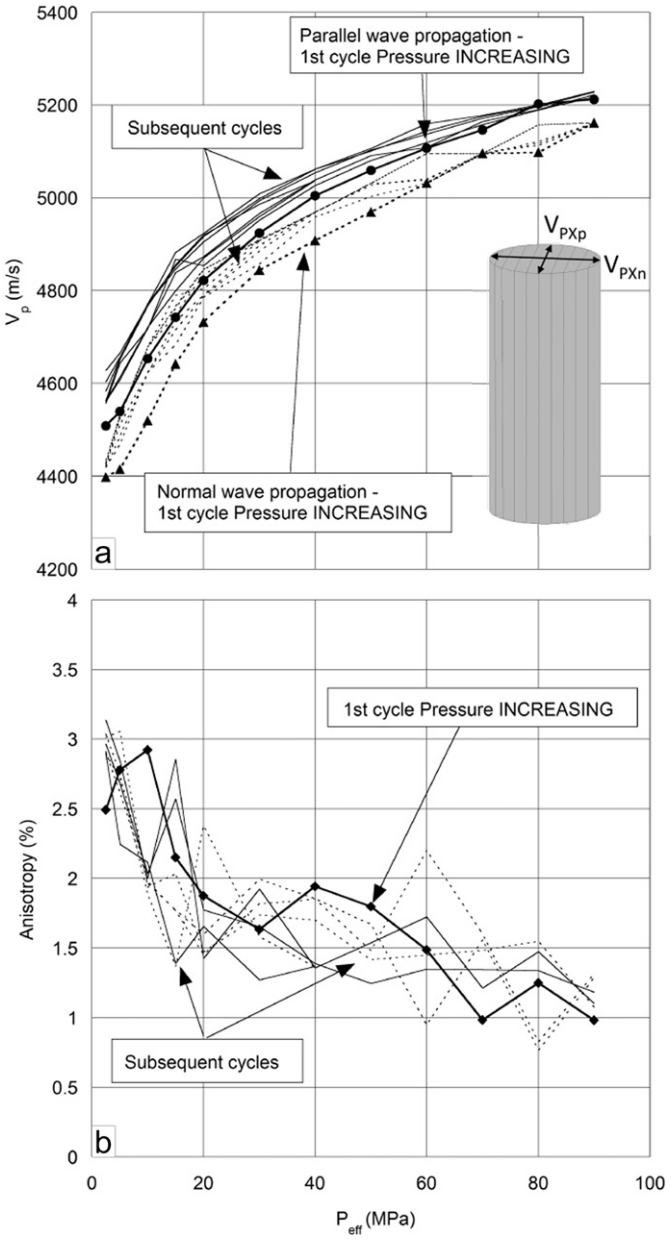

Fig. 6. Compressional elastic wave velocities measured across the diameter under elevated effective pressure and saturated conditions. Panel (a): V_P parallel and normal to bedding for COS_x, Panel (b) A_V for COS_x – for effective pressure increasing (solid lines), effective pressure decreasing (dotted lines). For clarity the initial increasing cycle is shown in black, subsequent variation in grey.

Table 2
Evolution of elastic wave velocities as function of P_C.

	V_{PXp}	V_{PXn}	V_{PX} - anisotropy
Initial	4526 m/s	4398 m/s	2.8%
At max Pc	5224 m/s	5212 m/s	0.2%
Increase	16%	17%	−65%
Permanent increase	1.1%	0.7%	

In contrast to the elastic wave velocities, permeability shows the opposite behaviour with changing pressure conditions (Fig. 7). For both flow directions, permeability decreases with increasing effective pressure and increases when effective pressure is subsequently reduced. A further permeability reduction is induced by each subsequent pressure cycle. And, although permeability does recover to an extent, it does not reach its original value indicating a permanent reduction of permeability. While both flow directions show the same general behaviour, there are significant differences between the measurements for COS_x (Fig. 7a) and COS_z (Fig. 7b). The initial permeability parallel to bedding (k_x), with a value of 33×10^{-18} m^2, is one order of magnitude higher than normal to bedding (k_z) (2×10^{-18} m^2), a strong initial permeability anisotropy(A_k) of around 180% (Fig. 7c). This anisotropy reduces to approximately 10% during seasoning (pressure cycles), likely as a result of the differential permeability reductions for k_x and k_z. The total reduction of k_x is approximately 98% (final $k = 0.53 \times 10^{-18}$ m^2), somewhat higher than the reduction of 70% for k_z (final $k = 0.6 \times 10^{-18}$ m^2). However, regardless of bedding orientation, a similar final permeability value is measured after pressure cycling, hence a weak permeability anisotropy after seasoning. The most significant decrease (68%) of k_x occurs for an effective pressure increase from 5 to 40 MPa during the 1st pressure cycle followed by a 2nd significant decrease (59%) in the 3rd pressure cycle.

In general, permeability changes for fluid flow normal to bedding are more evenly distributed across the four pressure cycles (Fig. 7b). All cycles show the same behaviour with a more rapid decrease of k_z up to 30 MPa, followed by a more gentle reduction with a continuously decreasing rate up to the maximum effective pressure. The permeability further decreases with each subsequent cycle. The minimum permeability is reached for both flow directions after approximately 3 pressure cycles, with further pressure cycles not significantly reducing permeability, as illustrated by the 4th pressure cycle, which has only a marginal absolute effect on k_x and k_z.

The time needed at every pressure step from the onset of pressure change, to the point where a new steady state flow is attained is defined as equilibration time (t_e), and is an important parameter in order to quantify the permeability hysteresis. Equilibration time data for both flow directions are presented in Fig. 8. For fluid flow parallel to bedding (Fig. 8a), the general trend of t_e is to increase with increasing pressure: from an average of 13 min at low effective pressure to an average of 24 min at maximum effective pressure, and with no significant

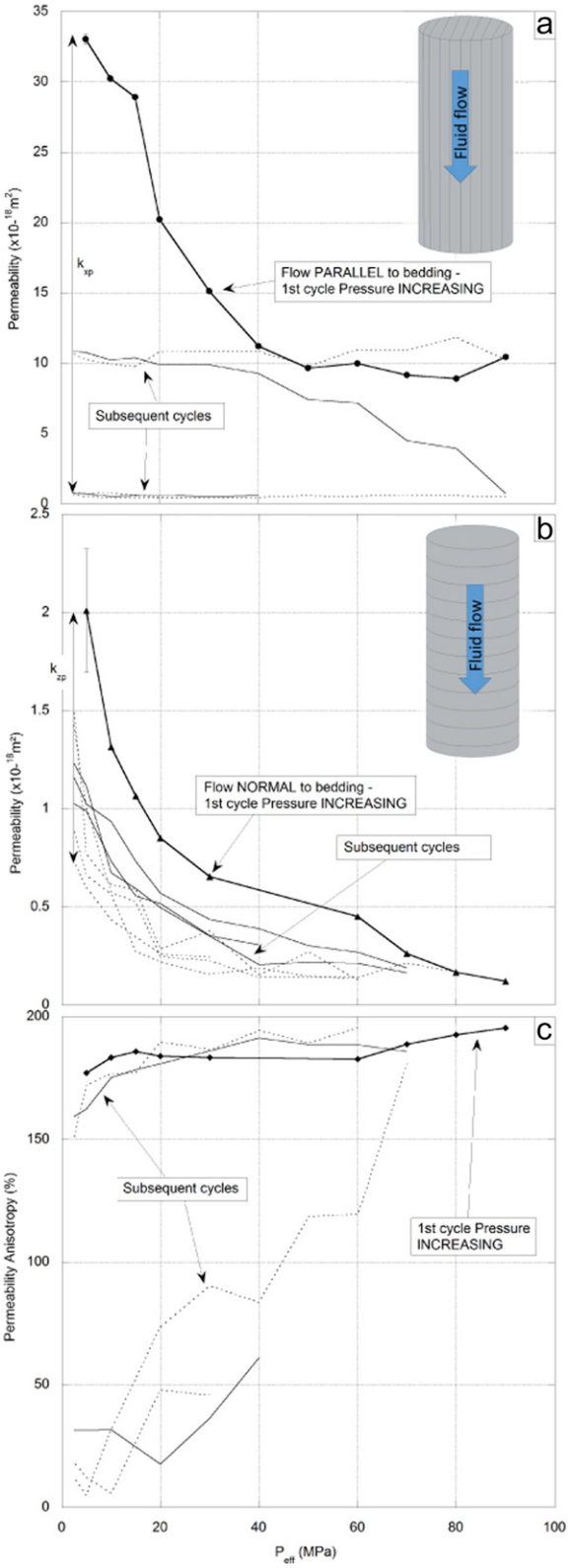

Fig. 7. Permeability and Permeability Anisotropy evolution over an effective pressure range up to 90 MPa; k_{xp} and k_{zp} indicating the permanent permeability change – (a) k_x, (b) k_z, (c) A_k. Effective pressure increase is shown with solid lines, decrease with dotted lines, and with the initial increase as a thick black line.

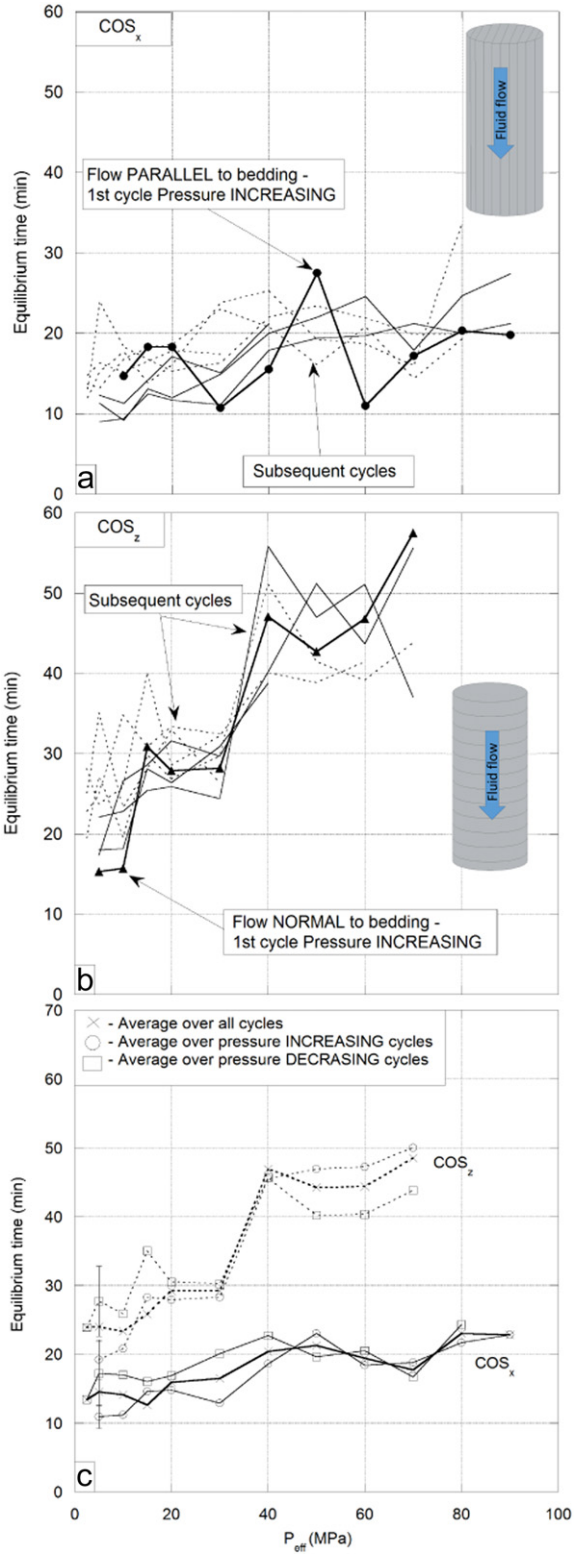

Fig. 8. Equilibrium time as function of effective pressure – for parallel (a) and normal (b) to bedding orientation for effective pressure increasing (solid lines) and effective pressure decreasing (dotted lines). Panel (c) summarises these data using a simple average at each pressure step.

difference between the pressure cycles. However, for the effective pressure range from 5 to 50 MPa, average t_e measured for cycles of decreasing pressure is slightly higher compared when the pressure is increasing, whereas at higher effective pressures equilibration times are similar. The trend of increasing equilibrium time with increasing effective pressure is more significant for fluid flow normal to bedding (Fig. 8b), with more time needed to equilibrate compared to COS_x. Here, the average t_e doubles from 24 min to 48 min over the tested pressure

range. As before at low effective pressures, average equilibrium times tend to be higher when effective pressure is decreased compared to when it is increased. However, this behaviour switches for effective pressures above 40 MPa, which is different to COS_x for this pressure range (Fig. 8c).

Finally, axial deformation was recorded during permeability measurements. A permanent axial strain (ε_{ap}) of 0.03% is determined for COS_x (Fig. 9a), with maximum axial strain (ε_a) of 0.12% at the maximum effective pressure. The axial strain is close to linear for each pressure cycle, with the largest deformation occurring during the first cycle. Afterwards, and for each subsequent pressure cycle, the deformation rate is low and little deformation occurs. A similar deformation pattern can be seen for COS_z but with significant differences in the absolute figures. Here, permanent and maximum axial strain for COS_z (Fig. 9b), are 0.05% and 0.26% respectively: almost twice that of COS_x. Fig. 9(c) shows a comparison of the average axial strain for COS_x and COS_z including the strain anisotropy. The initial axial strain anisotropy is 30% at low effective pressure and increases to a maximum of about 80% at 20 MPa and does not change significantly with further pressure increase. The same trend is seen for decreasing effective pressure: the axial strain anisotropy stays relatively constant and starts decreasing at 20 MPa down to the minimum effective pressure. Subsequent cycles show a similar general behaviour, but with smaller absolute deformation and very little change of the anisotropy between cycles.

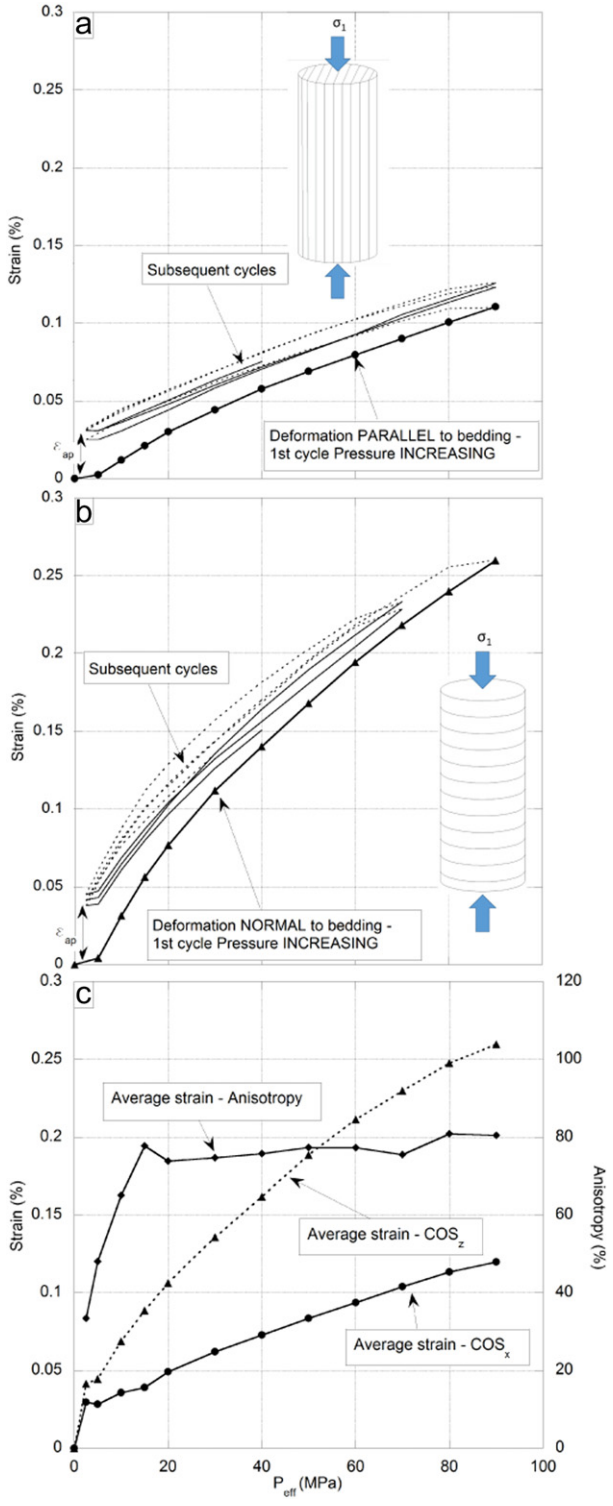

Fig. 9. Axial strain and Strain Anisotropy evolution over an effective pressure range up to 90 MPa; ε_{ap} indicates the permanent deformation – for (a) parallel to bedding and (b) normal to bedding, and with pressure increasing shown by solid lines and, effective pressure decreasing (dotted lines).

5. Discussion

Results of elastic wave measurements under ambient pressure conditions show that COS is highly anisotropic. The direction of the maxima measured V_P aligned well with the direction of the observed cross-bedding. In contrast, the minima was measured perpendicular relative to the cross-bedding. The anisotropic velocity (between 10% and 27%) suggests a planar anisotropy parallel to bedding, with the maximum principal velocity axis lying parallel to inherent cross-bedding.

Triaxial compression experiments for both directions reveal a prominent strength anisotropy of 18%, similar to the elastic wave anisotropy. Crab Orchard Sandstone is considerably stronger when compressed with the deformation axis, i.e. direction of σ_1, normal to bedding (208.9 MPa peak strength) compared to the deformation axis parallel to bedding (174.1 MPa peak strength). However, COS_x has a higher stiffness (49.3 GPa) than COS_z (43.9 GPa). This behaviour may be understood by examining the strain of the two samples. Whereas COS_x showed a larger diametric deformation, COS_z exhibited a larger axial deformation (Fig. 10). The difference in deformation behaviour is also shown by the significant difference in the Poisson's ratio (0.31 for COS_x compared to 0.11 for COS_z). This distinct anisotropic deformational behaviour suggest that the deformation of the samples is also influenced by the inherent bedding (not just velocity/permeability). Therefore, the extent of deformation in any one direction depends on the principal stress orientation relative to inherent bedding. For COS_z, the bedding planes are likely acting as a strengthening framework, preventing a radial deformation and channelling the axial stress in an axial direction and enhancing a compression of the intervals between the bedding planes, generating a dominant axial deformation. The opposite can be seen for COS_x, where the radial strain is dominant. The resultant behaviour during deformation may be simplified as a beam stability problem by considering the intervals between the bedding planes as columns. Here, the deformation may be compared to flexure buckling, a sideways deformation of columns, which is a common phenomenon in disciplines such as engineering geology (Silva and Lana, 2014; Liu et al., 2016). As axial stress (σ_1) increases at constant confining pressure (σ_3), bedding planes are likely to deform as they deflect the axial stress and promote radial deformation of the sample. Following this, a likely explanation for the higher stiffness of COS_x compared to COS_z is the lower axial (vertical) stress required for the compression of the intervals between the bedding planes (COS_z) compared to the stress required to *deform* those bedding planes against the (lateral) confining pressure. Such a process is further likely to weakening the contact between the bedding planes and the rock matrix in between the planes, leading to the lower peak strength of COS_x.

In addition, the alignment of bedding planes with direction of σ_1 for COS_x is also likely to promote the nucleation of micro fractures along bedding planes. Specifically, when deforming COS_x, micro-fractures

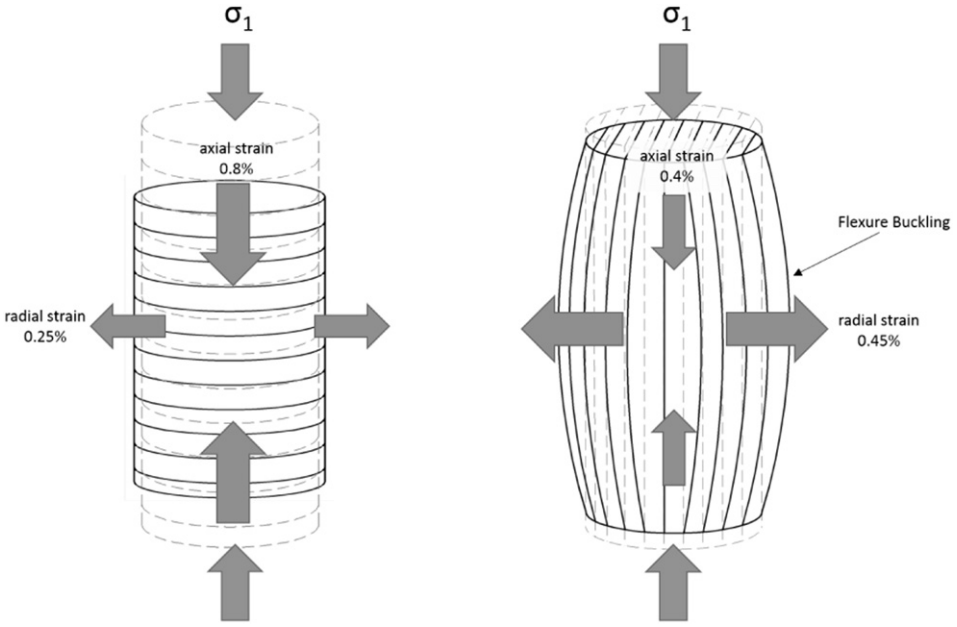

Fig. 10. Schematic of axial deformation, larger arrows indicating the preferred direction of deformation.

are initially initiated at a low angle to the maximum principle stress, but are then deviated when encountering the bedding planes. In Contrast, the fracture pattern for COS_z supports this idea, showing two fractures in an "X"-shape, both at $\approx 30°$ to σ_1. Strength anisotropy is therefore likely to be predominantly controlled by the orientation of the major stress direction (σ_1) relative to the inherent bedding.

Porosity decreases as a function of effective pressure for both samples, COS_x and COS_z but with a different reduction pattern and magnitude. Porosity in COS_x reduces rapidly up to 20 MPa during the first cycle becoming almost linear at higher pressures and in subsequent pressure cycles. In contrast, COS_z shows a linear and more gradual reduction in porosity over the entire pressure range and all pressure cycles. However, the biggest difference can be seen in the magnitude of porosity or pore volume reduction. This could be due to the fluid flow direction or direction of deformation relative to bedding or a combination of both. This results in a much higher permanent reduction of porosity/pore volume for fluid flow/deformation parallel to bedding, approximately 85% compared to just 30% when fluid flow and deformation is normal to bedding. These observations indicate that the porosity change is greatly influenced by the orientation of bedding planes. This effect is reflected in the deformational behaviour and the change in velocity, which is entirely consistent with the well-known link between the porosity of a porous medium and elastic wave velocity, which is known to be significantly affected by pore fluids (Guéguen and Schubnel, 2003; Benson et al., 2005; Fortin et al., 2011). For the experiments reported here, despite the much lower reduction in porosity in COS_z, the increase in V_P parallel to bedding was approximately the same in both samples. A pore volume decrease of approximately 60% in COS_x over the pressure range 2.5–90 MPa during the 1st pressure cycle resulted in an increase of V_{PXp} and V_{PXn} of 16% and 17% respectively. Whereas, in COS_z, a decrease in porosity of only 12% during the 1st cycle leads to a comparable increase in V_{PZp} of around 17%. It is interesting, that despite further pore closure during the subsequent pressure cycles, compressional wave velocity does not change significantly between the pressure cycles. This indicates, that additional pore closure does not increase conductivity further. In terms of anisotropy, it is clear from our data that V_P-anisotropy (at 2.5%–3%) is significantly lower at elevated pressures compared to anisotropy measured at ambient conditions (19%), and decreases with increasing effective pressure (to around 1% at 90 MPa P_{eff}, Fig. 6b). It is therefore likely that this permanent pore volume decrease in both samples (85% and 30%) is tied to an inherent plastic (non-recoverable) deformation, caused by irreversible closures of micro cracks and pores (Wang and Xu, 2013), and aided by the clay-rich nature of this material.

It is clear that sample permeability changes significantly as a function of both pressure and flow direction relative to the orientation of the bedding. Initially, micro-cracks and open pores form a relatively easy pathway for fluid flow, either normal and parallel to bedding. For fluid flow parallel to bedding, the bedding planes act as additional conduits for fluid flow, which would explain the relatively high permeability (k_x, 33×10^{-18} m^2), an order of magnitude higher than for fluid flow normal to bedding (k_z, 2×10^{-18} m^2), where bedding planes act as barriers. Such information is particularly applicable to field cases involving laminated rocks, such as shale or mudrock with fine layering, and how these respond to hydraulic stimulation. Knowledge of the stress path and evolution of permeability is useful for such scenarios where multiple instances of stimulation may be used – our data support the hypothesis of diminishing returns of permeability enhancement (e.g. Fig. 7) when dealing with cyclical pore pressure variation. The initial permeability anisotropy (180%) is far higher than for elastic wave velocities. However, the directions of the maximum and minimum flow are in good agreement with the principal directions indicated by V_P, as supported by previous data (Benson et al., 2003; Benson et al., 2005).

For the initial pressure cycles, permeability anisotropy changes little, suggesting that fluid flow is reduced by the same relative amount independently of flow direction. The observation of the wave velocity anisotropy, which is heavily influenced by cracks, further supports the notion that the void space in COS contains a significant crack component (Guéguen and Schubnel, 2003; Benson et al., 2005; Fortin et al., 2011). However, by the time of the third pressure cycle, permeability anisotropy has significantly reduced to a minimum of around 10%. Therefore, with subsequent pressure cycles, fluid flow parallel to bedding is more significantly reduced, finally reaching permeability values very similar to k_z after pressure cycling. This behaviour is typical for a predominantly planar fabric with a pore structure composed of interconnected low aspect ratio, elongated pores (Jones et al., 1998). The permeability evolution and the change in anisotropy leads to the suggestion that the open pores are therefore a mixture of low aspect ratio, elongated pores and equant, higher aspect ratio pores (Jones et al., 1998), which are not closing simultaneously and therefore causing

two distinct phases of permeability reduction. In the first phase, the low aspect ratio cracks and low aspect ratio pores close permanently (and are effectively closed at hydrostatic pressure above ~40 MPa). The permeability data imply that pores are elongated parallel to bedding and therefore easy to close (Jones et al., 1998). This reduces fluid flow independently of flow direction, hence permeability anisotropy remains constant. The remaining relatively high permeability (in the case of COS_x) may therefore be explained as a series of high aspect ratio pores remaining open and therefore presenting flow paths in combination with bedding planes orientated parallel to the imposed fluid flow. This flow path is not present in COS_z, as the bedding planes present an additional barrier to fluid flow. The second phase is characterised by the closure of equant and high aspect ratio pores, which affects k_x more than k_z, and leading to a significant reduction of permeability anisotropy from around 180% to 10%. Porosity evolution further supports this hypothesis. In the first phase, during the closure of crack type and low aspect ratio pores, a relatively high reduction in pore volume in both samples is seen, whereas during the second phase, COS_x shows a much higher reduction in pore volume compared to COS_z. From the behaviour of permeability and permeability anisotropy, we deduce that crack type and low aspect ratio pores form the major part of the COS microstructure and equant, high aspect ratio pores exist to a lesser extent (also supported by SEM data).

At low effective pressure the equilibrium time for fluid flow normal to bedding (t_{ez}) is twice as high as t_{ex}, increasing to almost three times at the maximum effective pressure (Fig. 8). Here, a shift is seen when comparing average t_e for increasing and decreasing effective pressure directions and for fluid flow parallel and normal to bedding (Fig. 8c), especially in the range 40–50 MPa. This is important, as it correlates well with the pressure at which most of the permeability reduction takes place. For bedding parallel, and fluid flow below 50 MPa effective pressure, the average t_e is higher for decreasing pressure compared to increasing pressure. Conversely, at higher effective pressures, equilibration times are almost equal (Fig. 8c). A similar shift occurs for bedding normal fluid flow at 40 MPa effective pressure. Here, at lower effective pressure, average equilibrium times are generally higher as effective pressure is decreased, which changes to the opposite for higher effective pressure. An analysis of the time required to establish equilibrium at every pressure step suggests that equilibrium time is dependent on the interaction between the anisotropy of the rock, and the effective stress state. Importantly, however, this parameter appears to be little influenced by stress history or permeability, as indicated by the similar time values for all pressure cycles (Fig. 7).

Frictional sliding, occurring at favourable configurations of cracks and pores during loading, may also explain the hysteresis (stress-path dependency) phenomenon we measure, likely due to cracks and pores not fully recovering to their original state during the unloading cycle (Bernabé, 1987). This process would lead to an irreversible change in rock properties due to the reduction of void space, and is backed up by the permanent change of permeability, porosity and acoustic wave velocity data seen in the data reported here. However, the presence of clay particles and associated pore clogging is also likely to contribute to a rapid (and irreversible) reduction in permeability early in the pressure cycling, making separation of these two effects difficult. Despite this, the mild but constant reduction of permeability with each subsequent pressure cycle suggests a continuing gradual closure of pores and cracks, which might be through a combination of compaction and frictional sliding (Selvadurai and Glowacki, 2008).

6. Conclusions

This study reports new data on the effects of stress-history, effective pressure and anisotropy on fluid permeability in a well cemented, anisotropic sandstone. Results showed that an irreversible, and cumulative change in permeability, porosity and acoustic wave velocity occurs with each pressure cycle, clearly indicating a stress-path dependency or hysteresis effect. Fluid flow parallel to bedding showed a particularly strong hysteresis. We identify two key phases for the permeability reduction as a function of effective pressure and strain. The first phase is characterised by a rapid decline of fluid flow reflecting the closure of low aspect ratio and crack type pores. The second phase characterises a slower permeability reduction via the more equant porosity. Taken together, low aspect ratio and crack type pore types are likely to dominate hydraulic connectivity, hence a rapid and substantial permeability reduction irrespectively of fluid flow direction.

We also conclude that it is likely that inelastic effects are generally caused by the cementation of the rock fabric, which in turn is heavily influenced by the way the pore space is organised (i.e. the mm-scale cross bedding that results in the strong anisotropy). It is therefore likely that a combination of different mechanisms must be taken into account in determining how tight sandstones react to burial and cyclical pressurisation. Such effects are likely not constrained to clayey sandstones, but to any low permeability, anisotropic rock formations such as shale, tight sandstone and carbonate rocks. It is clear that fluid conductivity of these reservoir rocks is likely been modified as the rock mass is transited through a complex stress-time history due to geological burial/uplift, and/or modification of pore pressure over time. Consequently, the movement of oil and gas, highly dependent on permeability, is likely to be significantly affected by stress history in addition to the current stress environment as well as the microstructure of the rock mass and inherent anisotropy. These results will help our understanding on how anisotropic, low permeability reservoirs respond to hydraulic stimulation, especially where multiple stimulation phases are used. Therefore, our improved understanding of the complex physics of fluid flow and stress and rock matrix dependent changes of the permeability could lead to improvements for oil and gas extraction, as well as other fields of applied geoscience.

Appendix A. Supplementary data

Supplementary data to this article can be found online at http://dx.doi.org/10.1016/j.tecto.2017.06.014.

References

Amadei, B., 1982. The Influence of Rock Anisotropy on Measurement of Stresses in Situ.
Bai, M., et al., 1999. Analysis of stress-dependent permeability in nonorthogonal flow and deformation fields. Rock Mech. Rock. Eng. 32 (3), 195–219.
Bennion, D., et al., 1996. Low permeability gas reservoirs: problems, opportunities and solutions for drilling, completion, stimulation and production. SPE Gas Technology Symposium.
Benson, P.M., 2004. Experimental Study of Void Space, Permeability and Elastic Anisotropy in Crustal Rocks Under Ambient and Hydrostatic Pressure.
Benson, P.M., Meredith, P.G., Platzman, E.S., 2003. Relating pore fabric geometry to acoustic and permeability anisotropy in Crab Orchard Sandstone: a laboratory study using magnetic ferrofluid. Geophys. Res. Lett. 30 (19).
Benson, P., et al., 2005. Pore fabric shape anisotropy in porous sandstones and its relation to elastic wave velocity and permeability anisotropy under hydrostatic pressure. Int. J. Rock Mech. Min. Sci. 42 (7), 890–899.
Benson, P.M., Meredith, P.G., Schubnel, A., 2006. Role of void space geometry in permeability evolution in crustal rocks at elevated pressure. J. Geophys. Res. Solid Earth 111 (B12).
Bernabé, Y., 1987. The effective pressure law for permeability during pore pressure and confining pressure cycling of several crystalline rocks. J. Geophys. Res. Solid Earth 92 (B1), 649–657.
Brace, W., Walsh, J., Frangos, W., 1968. Permeability of granite under high pressure. J. Geophys. Res. 73 (6), 2225–2236.
David, C., et al., 2001. Mechanical compaction, microstructures and permeability evolution in sandstones. Phys. Chem. Earth Solid Earth Geod. 26 (1), 45–51.
Fortin, J., et al., 2011. Influence of thermal and mechanical cracks on permeability and elastic wave velocities in a basalt from Mt. Etna volcano subjected to elevated pressure. Tectonophysics 503 (1), 60–74.
Guéguen, Y., Palciauskas, V., 1994. Introduction to the Physics of Rocks. Princeton University Press.
Guéguen, Y., Schubnel, A., 2003. Elastic wave velocities and permeability of cracked rocks. Tectonophysics 370 (1), 163–176.
Hadley, K., 1976. The effect of cyclic stress on dilatancy: Another look. J. Geophys. Res. 81 (14), 2471–2474.

Jones, C., Meredith, P., et al., 1998. An experimental study of elastic wave propagation anisotropy and permeability anisotropy in an illitic shale. SPE/ISRM Rock Mechanics in Petroleum Engineering.
Keaney, G., et al., 1998. Laboratory study of permeability evolution in a tight' sandstone under non-hydrostatic stress conditions. SPE/ISRM Rock Mechanics in Petroleum Engineering.
Keaney, G.M., et al., 2004. Determination of the effective stress laws for permeability and specific storage in a low porosity sandstone. Gulf Rocks 2004, the 6th North America Rock Mechanics Symposium (NARMS).
Lion, M., Skoczylas, F., Ledésert, B., 2004. Determination of the main hydraulic and poroelastic properties of a limestone from Bourgogne, France. Int. J. Rock Mech. Min. Sci. 41 (6), 915–925.
Liu, H., Wang, G., Huang, F., 2016. Methods to analyze flexural buckling of the consequent slabbed rock slope under top loading. Math. Probl. Eng. 2016.
Meyer, R., 2002. Anisotropy of sandstone permeability. CREWES Research Report. 14, pp. 1–12.
Sammonds, P., 1999. Understanding the fundamental physics governing the evolution and dynamics of the Earth'crust and ice sheets. Philos. Trans. R. Soc. Lond. A 357 (1763), 3377–3401.
Scholz, C., Koczynski, T., 1979. Dilatancy anisotropy and the response of rock to large cyclic loads. J. Geophys. Res. Solid Earth 84 (B10), 5525–5534.
Selvadurai, A., Glowacki, A., 2008. Permeability hysterisis of limestone during isotropic compression. Groundwater 46 (1), 113–119.
Shiping, L., et al., 1994. Permeability-strain equations corresponding to the complete stress—strain path of yinzhuang sandstone. International Journal of Rock Mechanics and Mining Sciences & Geomechanics Abstracts, pp. 383–391.
Silva, C.H.C., Lana, M.S., 2014. Numerical modeling of buckling failure in a mine slope. REM Revista Escola de Minas 67 (1), 81–86.
Spiteri, E.J., et al., 2008. A new model of trapping and relative permeability hysteresis for all wettability characteristics. SPE J. 13 (03), 277–288.
Wang, H., Xu, W., 2013. Relationship between permeability and strain of sandstone during the process of deformation and failure. Geotech. Geol. Eng. 31 (1), 347–353.
Zoback, M.D., Byerlee, J.D., 1975a. The effect of cyclic differential stress on dilatancy in Westerly granite under uniaxial and triaxial conditions. J. Geophys. Res. 80 (11), 1526–1530.
Zoback, M.D., Byerlee, J.D., 1975b. The Effect of Microcrack Dilatancy on the Permeability of Westerly Granite.